Tellus SERIES B CHEMICAL AND PHYSICAL METEOROLOGY
PUBLISHED BY THE INTERNATIONAL METEOROLOGICAL INSTITUTE IN STOCKHOLM

Tellus (2009), 61B, 118–130

TELLUS

Saharan dust absorption and refractive index from aircraft-based observations during SAMUM 2006

By ANDREAS PETZOLD[1]*, KATHARINA RASP[1], BERNADETT WEINZIERL[1], MICHAEL ESSELBORN[1], THOMAS HAMBURGER[1], ANDREAS DÖRNBRACK[1], KONRAD KANDLER[2], LOTHAR SCHÜTZ[3], PETER KNIPPERTZ[3], MARKUS FIEBIG[4] and AKI VIRKKULA[5], [1]*Deutsches Zentrum für Luft- und Raumfahrt, Institut für Physik der Atmosphäre, Oberpfaffenhofen, 82234 Wessling, Germany;* [2]*Applied Geosciences Department, Darmstadt University of Technology, 64287 Darmstadt, Germany;* [3]*Institute for Atmospheric Physics, Johannes Gutenberg-University, 55099 Mainz, Germany;* [4]*Department for Atmospheric and Climate Research, Norwegian Institute for Air Research, Kjeller, Norway;* [5]*Finnish Meteorological Institute, Air Quality Research, 00560 Helsinki, Finland*

(Manuscript received 19 December 2007; in final form 29 July 2008)

ABSTRACT

During the Saharan Mineral Dust Experiment (SAMUM) conducted in summer 2006 in southeast Morocco, the complex refractive index of desert dust was determined from airborne measurements of particle size distributions and aerosol absorption coefficients at three different wavelengths in the blue (467 nm), green (530 nm) and red (660 nm) spectral regions. The vertical structure of the dust layers was analysed by an airborne high spectral resolution lidar (HSRL). The origin of the investigated dust layers was estimated from trajectory analyses, combined with Meteosat 2nd Generation (MSG) scenes and wind field data analyses. The real part n of the dust refractive index was found almost constant with values between 1.55 and 1.56, independent of the wavelength. The values of the imaginary part k varied between the blue and red spectral regions by a factor of three to ten depending on the dust source region. Absolute values of k ranged from 3.1×10^{-3} to 5.2×10^{-3} at 450 nm and from 0.3×10^{-3} to 2.5×10^{-3} at 700 nm. Groupings of k values could be attributed to different source regions.

1. Introduction

Radiative forcing by soil dust particles is complex, since dust particles not only scatter but also partly absorb incoming solar radiation, and the particles absorb and emit outgoing long-wave radiation. The magnitude and even the sign of the dust radiative forcing depend on the optical properties of the dust, on its vertical distribution, on the presence of clouds and on the albedo of the underlying surface (Sokolik and Toon, 1996; Tegen et al., 1996; Liao and Seinfeld, 1998; Myhre and Stordal, 2001). An indispensable prerequisite for estimating the radiative effects and interactions of dust and climate is the quantification of atmospheric dust loads and the determination of size-dependent optical properties of the dust particles.

Data of dust optical properties are either taken from laboratory measurements (Patterson et al., 1977; Shettle and Fenn, 1979; d'Almeida et al., 1991; Sokolik et al., 1998; Sokolik and Toon, 1999; Lafon et al., 2006; Linke et al., 2006) or are determined from optical or satellite retrievals (e.g. Dubovik et al., 2002; Cattrall et al., 2003; Todd et al., 2007). Although it is one of the key parameters controlling dust optical properties, the imaginary part of the complex refractive index is uncertain and varies from $<1 \times 10^{-3}$ to 0.01 for a wavelength of 550 nm. Recent studies (Dubovik et al., 2002; Balkanski et al., 2007; Todd et al., 2007) have demonstrated that the values commonly used for the imaginary part of the refractive index (Patterson et al., 1977; Shettle and Fenn, 1979; d'Almeida et al., 1991) are overestimating aerosol light absorption. The variability of the imaginary part of the complex refractive index depends crucially on the iron content and on its mineralogical phase (Alfaro et al., 2004; Lafon et al., 2006; Linke et al., 2006).

Dust optical properties used in large-scale models are assumed to be constant in space and time, ignoring that dust from different source regions may have different optical properties, that the optical properties may vary with particle size and that the optical properties may be modified during the atmospheric transport. Among the few in situ data on dust optical properties from airborne measurements, the Saharan Dust Experiment

*Corresponding author.
e-mail: andreas.petzold@dlr.de
DOI: 10.1111/j.1600-0889.2008.00383.x

(SHADE; Tanré et al., 2003) research flights encountered one Saharan dust outbreak event in the Cape Verde region in 2000. The single-scattering albedo measured during SHADE is 0.96–0.97 at 550 nm (Haywood et al., 2003), which agrees with recent values of 0.95–0.98 from laboratory studies (Linke et al., 2006). The SHADE team clearly states that they investigated only unpolluted dust aerosol, which has a net cooling effect over sea (Tanré et al., 2003). Earlier measurements provided a value of 0.87 (Haywood et al., 2001), which is likely to be so low due to mixing with absorbing biomass-burning aerosol. Pointing in the same direction, dust coated with carbonaceous aerosol observed during ACE-Asia also leads to increased absorption of solar radiation (Bergstrom et al., 2004).

During the Saharan Mineral Dust Experiment (SAMUM; Heintzenberg, 2008), the research aircraft Falcon 20-E of the German Aerospace Centre (DLR) was operated, carrying a comprehensive set of aerosol instrumentation and a high spectral resolution lidar (HSRL). The in-depth analysis of the variability and characteristics of dust size distributions is presented by Weinzierl et al. (2008). The novel airborne HSRL and first results obtained during SAMUM are described in Esselborn et al. (2008). Our study focuses on the determination of the complex refractive index of dust particles originating from different source regions. For this purpose, we analysed aerosol absorption data measured by a three-wavelength Particle Soot Absorption Photometer (PSAP; Virkkula et al., 2005) and particle size distribution data using a highly sophisticated data analysis algorithm developed by Fiebig et al. (2005). The different dust episodes encountered during SAMUM permit the investigation of the influence of source regions across the northwestern Sahara as well as the mobilization processes on dust optical properties and their variability. Comparisons with optical properties derived from chemical analyses of collected dust samples (Kandler et al., 2008) are used for the evaluation of our method.

2. Methods

During the SAMUM core phase, three large-scale dust episodes extended from southern Morocco to Portugal. The dust episodes are referred to as Episode 1, on 19–22 May 2006, Episode 2, on 27–30 May, and Episode 3, on 3–4 June. Maximum aerosol optical thicknesses (AOT) at 500 nm measured by AERONET sun photometers at Ouarzazate (Tesche et al., 2008) were 0.6 (20 May), 0.6 (27–28 May) and 0.7 (3 June). During Episodes 1 and 2, the dust layer was composed of relatively homogeneous air masses, whereas during Episode 3 the layer clearly showed a stratified structure with different characteristics.

Detailed meteorological analyses (Knippertz et al., 2008) and lidar data analyses (Tesche et al., 2008) characterise the episodes as dominated by locally generated dry-convective dust plumes associated with high surface and air temperatures (Episode 1), by variable dust conditions, partially associated to strong thunderstorms and high wind speeds (Episode 2), and by strong easterly flow of dusty air associated with a cold surge into northeastern Algeria and Tunisia (Episode 3).

The average geometric thickness of the observed dust layers was 4.0 ± 0.9 km (Weinzierl et al., 2008). At the Ouarzazate site, the dust events on 18–22 and 27–28 May on one hand and starting at 3 June on the other hand, were well separated by a clean air episode (AOT < 0.1 on 29–30 May; Tesche et al., 2008). At the Tinfou site near Zagora, however, AOT did not vary that strong between different episodes, which may be due to the close vicinity to the desert (Knippertz et al., 2008). During these episodes, local research flights in the Ouarzazate–Zagora area were conducted on 19/20/22 May, 28 May and 3/4 June. An overview of the entire data set and all performed flights is given by Weinzierl et al. (2008). Knippertz et al. (2008) present a detailed analysis of the meteorological conditions during SAMUM and potential dust source regions.

2.1. Instrumentation and sampling strategy

The Falcon in situ instrumentation used here consisted of different aerosol sizing instruments, which covered the particle size range from 4 nm to 100 μm in diameter (D_p). Instruments sensitive to the sub-μm fraction were operated inside the aircraft cabin whereas optical sizing instruments covering the size range up to 100 μm in diameter were operated at wing stations. Aerosol absorption was measured at wavelengths 467, 530 and 660 nm, by means of a three-wavelength PSAP Bond et al., 1999; Virkkula et al., 2005). The PSAP was operated at a flow rate of 2.0 L min^{-1}, with filters being changed after every flight. Lowest observed filter transmittances were 0.70. The volume fraction of the aerosol volatile component was measured with a new instrument configuration consisting of several Condensation Particle Counters (CPC), which were partially equipped with diffusion screen separators (Feldpausch et al., 2006) and another optical particle counter. Connecting this instrument combination to a thermal denuder, the size-resolved analysis of the non-volatile aerosol fraction was possible. The vertical distribution of the dust particles and the aerosol extinction coefficient were measured by means of a nadir-looking HSRL (Esselborn et al., 2008).

For this study, we used data from a passive cavity aerosol spectrometer probe (PCASP-100X; $0.1 < D_p < 3.0\,\mu$m) and a forward scattering spectrometer probe (FSSP 300; $0.3 < D_p < 20\,\mu$m) mounted under the wing of the aircraft, as well as data from a GRIMM 1.109 optical particle counter ($D_p > 0.25\,\mu$m). The transfer function of the aerosol inlet was determined during the SAMUM flights. The GRIMM Optical particle counter (OPC) and the CPCs sampled from the same sampling line as the 3λ-PSAP, so that the size distribution of the particles collected by the PSAP filter was known. Since the aerosol absorption measurement via a PSAP was based on filter sampling downstream the aerosol inlet of the Falcon, the maximum particle size collected on the filter was limited to $\sim$3 μm in diameter (Petzold

et al., 2002). Therefore, the PSAP analysis provides refractive index information only for the so-called fine mode fraction of the aerosol with $D_p \leq 2.5\ \mu$m.

The combination of a nadir-looking airborne HSRL with in situ instrumentation permitted the precise guiding of the aircraft into distinct dust layers. The on-board recording of the lidar return signal identified the top of the dust layers, its thickness and the internal structure, that is, whether the layer was well mixed or consisted of stacked sublayers. The elevations of the selected layers were then given to the pilots who flew the aircraft into the dust layers for in situ sampling. Each layer was sampled at constant altitude for at least 5 min flight time (~40 km distance) to ensure sufficient particle statistics.

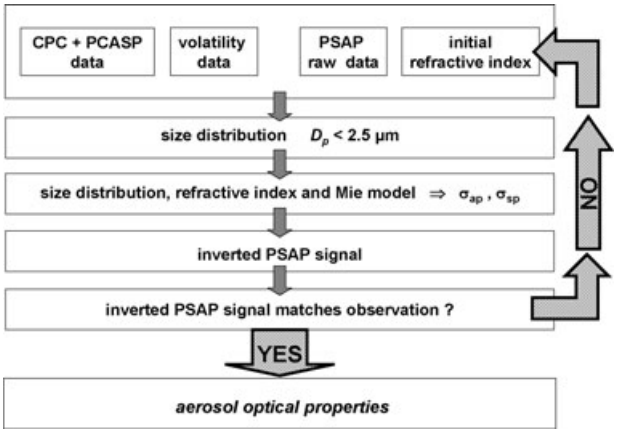

Fig. 1. Data analysis scheme.

2.2. PSAP data analysis

The PSAP data were used to infer dust absorption coefficients σ_{ap}. From previous experience (Petzold et al., 2002) only constant-altitude flight sequences were analysed. This reduction of data analysis avoids measurement artefacts due to pressure changes in the sampling line during ascent and descent of the aircraft between different flight levels. The data analysis used a 10-s moving average. This averaging time was found to smooth the data sufficiently while keeping the time-resolution at a required level. The detection limit of the method in terms of an absorption coefficient was set to 0.1×10^{-6} m^{-1} at standard conditions (273.14 K, 1013.25 hPa), based on experience from earlier studies (Petzold et al., 2002).

Two problems were encountered: (1) information about the refractive index is required in advance to interpret the optical particle counter data and (2) we have to apply scattering and filter loading corrections to deduce the absorption from the PSAP transmission signal. Spot-size and flow-correction followed Bond et al. (1999), whereas for the scattering correction, the revised correction factors proposed by Virkkula et al. (2005) were used. Since no direct measurement of the aerosol light scattering coefficient was available, the scattering coefficient was calculated from the particle size distributions by means of Mie theory. Uncertainties caused by the use of Mie theory are assumed to be small since the PSAP analyses dust collected on a filter matrix that represents an average over randomly oriented non-spherical particles, see also Section 3.1.2.

The required refractive index was determined from the spectral dependence of the absorption coefficient data. Figure 1 shows the iterative data analysis scheme. Number size distribution data from CPC and optical particle counters served as input data. The complex refractive index $m = n + ik$ of the composite particle was obtained from an effective medium mixing rule (Ackerman and Toon, 1981; Ouimette and Flagan, 1982). Volatility analyses (Weinzierl et al., 2008), hygroscopic growth analyses (Kaaden et al., 2008) and chemical analyses (Kandler et al., 2008) of aerosol samples yielded consistently that particles smaller than 0.35–0.5 μm contained a considerable volatile and hygroscopic fraction, whereas particles larger than 0.5 μm were almost entirely non-volatile and showed no significant humidity-related particle growth. According to the volatility analyses, an externally mixed volatile component was not considered in the Mie model.

For the calculation of the aerosol optical properties, the aerosol was assumed to consist of exclusively light scattering components ($(NH_4)_2SO_4$, SiO_2), of one light absorbing component with a weak spectral dependence of the absorption coefficient (BC, kaolinite) and of one light absorbing component with a strong spectral dependence of the absorption coefficient (haematite). The selected key components dominating dust optical properties follow the proposal of Sokolik and Toon (Sokolik and Toon, 1999). As is explained in detail in Section 3.3.2, it turned out that attributing dust absorption to haematite only cannot reproduce the observed spectral dependence of the aerosol absorption coefficient. The consideration of a spectrally flat absorber (BC, kaolinite) was necessary to model the observed instrument response.

We have to state very clearly that our method does not perform a chemical analysis of the dust particles. Rather, we had to select the proxy key compounds according to the availability of reliable spectrally resolved information on the complex refractive indices. An analysis of the existing data yielded the selected key representative compounds as best-possible choice.

There are two other possible ways forward to determine the complex refractive index: (1) to start with independent values for the real and the imaginary part without any link to chemical compounds and (2) to calculate the refractive index, based on the results from the chemical analysis. We decided against these two options since (1) real and imaginary parts are not independent in reality, so, we might end up with an unphysical combination of real and imaginary part and (2) particularly the volume fractions of light-absorbing compounds like haematite are very low and connected to large uncertainties; furthermore, not for all chemical compounds there are optical constants available. Therefore,

we decided to use the concept of key proxies, which is also used in global modelling (Sokolik and Toon, 1999).

Based on our volatility analyses, we assumed two zones with different main mineralogical components. The transition between the two zones varied from 0.35 to 0.5 μm. Anthropogenically influenced aerosol, with particles <0.5 μm (zone 1), was modelled by an internal mixture of quartz (SiO_2) and black carbon (BC), covered with a layer of ammonium sulphate ($(NH_4)_2\,SO_4$). Dust aerosol with particles >0.5 μm (zone 2) was modelled by an internal mixture of quartz, kaolinite and haematite.

The refractive index for each zone was calculated from the volume average value

$$m = \sum_j (n_j + \mathrm{i}k_j)v_j, \tag{1}$$

with $(n_j + \mathrm{i}k_j)$ being the complex refractive index and v_j the volume fraction of the j-th component of the particle. The volume fractions were determined by the iterative procedure described in the following. The wavelength dependence of the individual refractive indices was taken from Shettle and Fenn (1979), Arakawa et al. (1997) and Sokolik and Toon (1999). Although these sources are currently under discussion, we have to rely on them since no other data are available.

We used the refractive index to calculate the size distribution from the PCASP and CPC data. The starting value of $(n_j + \mathrm{i}k_j)$ was obtained from an assumed chemical composition of the aerosol, based on the above-mentioned key compounds. We then obtained average aerosol optical properties, particularly the absorption and the scattering coefficients σ_{ap} and σ_{sp}, respectively, by using the initial refractive index and the size distribution as input for a Mie code (Bohren and Huffman, 1983), including a coated sphere scheme (Toon and Ackerman, 1981). The absorption and scattering coefficients were used to calculate the inverted PSAP signal according to the common PSAP correction scheme

$$\sigma_{\mathrm{PSAP}} = K_1\sigma_{\mathrm{sp}} + K_2\sigma_{\mathrm{ap}}, \tag{2}$$

with factors K_1 and K_2 being wavelength-dependent (Bond et al., 1999; Virkkula et al., 2005). If the inverted PSAP signals at 467, 530 and 660 nm agreed within 3% with the observed PSAP signal, we considered the match sufficient for the determination of refractive index, size distribution and the optical properties. Otherwise the iterative procedure was repeated. Changing the refractive index in the next iteration step also shifted the threshold sizes of the channels of the PCASP, which is taken into account very carefully. Virkkula et al. (2006) applied a comparable approach during their study on Antarctic boundary layer aerosol, which is based on scattering coefficient data and chemical analyses of impactor samples.

The key parameter used in this study for the investigation of the wavelength-dependence of aerosol light absorption by dust is the absorption Ångström exponent $\mathring{a}_{\mathrm{ap}}$, which is defined as

$$\mathring{a}_{\mathrm{ap}} = -\frac{\ln[\sigma_{\mathrm{ap}}(\lambda = 467\,\mathrm{nm}, m, n(D_{\mathrm{p}}))/\sigma_{\mathrm{ap}}(\lambda = 660\,\mathrm{nm}, m, n(D_{\mathrm{p}}))]}{\ln(467/660)}, \tag{3}$$

where m describes the complex refractive index, $n(D_{\mathrm{p}})$ represents the particle size distribution. The definition is similar to the 'classical' extinction Ångström exponent (Angström, 1964), which is widely used in atmospheric optics. We recall that the PSAP method provides refractive index data only for the fine mode fraction size range, with $D_{\mathrm{p}} \leq 2.5\,\mu$m.

The key parameter describing the aerosol size distribution is the effective diameter defined as (McFarquhar and Heymsfield, 1998)

$$D_{\mathrm{eff}} = \frac{\int D_{\mathrm{p}}^3 n\left(D_{\mathrm{p}}\right) \mathrm{d}D_{\mathrm{p}}}{\int D_{\mathrm{p}}^2 n\left(D_{\mathrm{p}}\right) \mathrm{d}D_{\mathrm{p}}}. \tag{4}$$

Because of the transfer function of the aerosol inlet, the integration is restricted to $D_{\mathrm{p}} < 2.5\,\mu$m and the effective diameter is labelled as $D_{\mathrm{eff,fine\,mode}}$.

2.3. Chemical analysis of dust samples

Dust particles were collected by a miniature impactor system (Kandler et al., 2007) consisting of three two-stage cascade impactors with cut-off particle diameters of approximately 1 and 0.2 μm. The impactor was connected to the same inlet as the PSAP. Hence the maximum upper size of collected particles is 2.5–3.0 μm, see also Section 2.1. The particles were collected on pure-carbon adhesive tape attached to pure nickel foil for post-flight analyses.

For each sample, several hundred particles were analysed in a scanning electron microscope with an attached energy-dispersive X-ray analysis system. This measurement setup yields particle size, morphological features and the element chemical composition for each single particle. In total 11 500 single particles collected onboard the aircraft were investigated. From the chemical data a complex index of refraction was calculated using a model mineralogy consisting of six substances (quartz, a silicate mixture, haematite, calcite, rutile and sulphate). For details on the measurement procedures, data classification and calculation procedures we refer the readers to Kandler et al. (2008).

2.4. Source region estimate

Source regions of dust were estimated by using a combination of backward trajectories, meteorological analyses from the European Centre for Medium-Range Weather Forecasts (ECMWF), dust storm reports from the World Meteorological Organisation (WMO) and satellite imagery from Meteosat 2nd

Generation (MSG). In the first step, 8 d backward trajectories were calculated for a large number of constant flight levels along the Falcon flight track using the Lagrangian Analysis Tool (LAGRANTO, Wernli and Davies, 1997). The LAGRANTO computes trajectories based on operational T799/L90 ECMWF analyses, which are interpolated on a $0.5^\circ \times 0.5^\circ$ latitude–longitude grid. These trajectories provide horizontal and vertical positions along the pathway of the air parcel through the atmosphere. To specify a dust source region, we applied a minimum threshold pressure of 880 hPa for trajectories to be in contact with the surface. This corresponds to an altitude of about 1000 m a.s.l.

Furthermore, we computed the surface wind field in the potential source regions of dust at 10-m height above ground. Wind velocities exceeding a threshold value of $6.5\,\mathrm{m\,s^{-1}}$ at 10-m height above ground enable dust mobilization in the case of appropriate soil conditions (Tegen and Lacis, 1996). Dust mobilization is considered to be possible if the LAGRANTO trajectories are close to the ground, that is, $p > 880$ hPa, and the analysed surface wind speed at 10 m exceeds $6.5\,\mathrm{m\,s^{-1}}$. Finally, we exploited MSG satellite imagery products and WMO dust storm reports that indicate the occurrence of dust clouds and compared them with trajectories and ECMWF wind fields at the date of mobilization.

Summarizing, this composite of methods identifies a region as a potential source for measured dust plumes only if at the same time plume trajectories were close to the surface with $p > 880$ hPa, horizontal winds exceeded a threshold value of 5–$7\,\mathrm{m\,s^{-1}}$, MSG images showed dust clouds and WMO dust storm reports indicated an event in this region. This method, however, neglects influences of the varying terrain elevation and of deep boundary layer mixing that transports dust into layers well above 880 hPa (Knippertz et al., 2008). Although the presented method is purely qualitative, we may gain insight into potential dust source regions and atmospheric transport times for dust plumes probed by the Falcon along its flight track. The source regions determined from our analysis also provide useful information for the key issue of the study on a potential influence of source areas on dust optical properties.

3. Results

3.1. Evaluation of the refractive index inversion scheme

3.1.1. Particle properties influencing $\mathring{a}_{ap}$. According to eq. (3), for a fixed wavelength interval, the aerosol absorption coefficient σ_{ap}, and thus, the absorption Ångström exponent $\mathring{a}_{ap}$ depends on the size distribution and on the refractive index. When we observe differences in $\mathring{a}_{ap}$, we have to consider both the effects of particle size distribution and refractive index. Thus, we investigated the influence of both parameters on the obtained $\mathring{a}_{ap}$ values by considering the following cases: (1) the refractive index m is constant and the number size distribution is variable and (2) both parameters are variable.

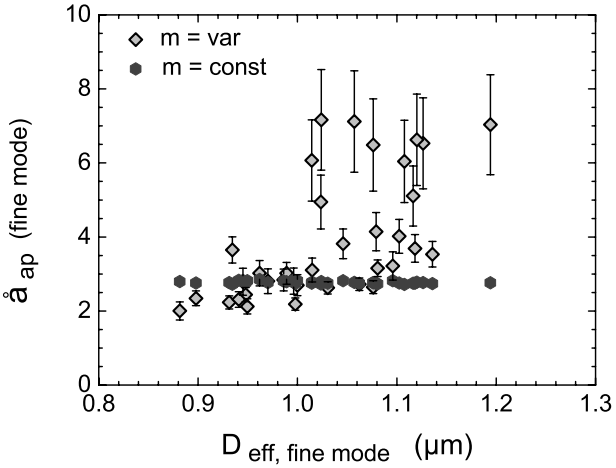

Fig. 2. Ångström exponent of absorption ($\mathring{a}_{ap}$) as a function of the effective diameter $D_{eff,fine\,mode}$ of the fine-mode aerosol ($D_p < 2.5\,\mu$m) collected by the PSAP filter; results refer to the data inversion allowing a variable refractive index (m = var) and to a test cases using the measured size distributions together with a fixed refractive index (m = const.) representative for dust samples with $\mathring{a}_{ap} < 3.0$.

These tests were performed using the averaged SAMUM fine-mode size distributions of all 37 analysed pure dust samples. Allowing the full variation of the refractive index, as obtained from the data inversion scheme, yields the data set shown in Fig. 2 by the open symbols. Although $D_{eff,fine\,mode}$ varies only by ±20% of the median value of 1.0 μm, $\mathring{a}_{ap}$ deduced from the PSAP data inversion varies from 2.0 to 7.0. Aerosol samples with $D_{eff,fine\,mode} < 1.0\,\mu$m do not vary significantly in $\mathring{a}_{ap}$, but for particle ensembles with $D_{eff,fine\,mode} > 1.0\,\mu$m, a separation into two subsets in terms of $\mathring{a}_{ap}$ is observed. To test whether this effect is dominated by the size distribution or by the refractive index, we reanalysed $\mathring{a}_{ap}$ for all samples with keeping the refractive index at a constant value of m (450 nm) = 1.56 + i 0.0042 and of m(700 nm) = 1.55 + i 0.0017, representing dust with a medium spectral dependence of σ_{ap}. The results are straightforward, providing a constant value of $\mathring{a}_{ap} = 2.73 \pm 0.03$, independent of the applied size distribution (filled symbols in Fig. 2).

The sensitivity study showed that for the analysed SAMUM dust cases, the imaginary part of the refractive index is almost exclusively responsible for the variability of the absorption Ångström exponent. The influence of the size distribution on the variation of $\mathring{a}_{ap}$ is nearly negligible for the studied dust samples. However, it has to be noted that this conclusion may be entirely invalid for aerosol with a larger variability in D_{eff} fine mode, in particular for aerosol samples containing large fractions of sub-μm-sized anthropogenic aerosol components.

3.1.2. Uncertainty of the refractive index inversion scheme. The results from the previous section can be used to estimate the uncertainty of the absorption Ångström exponent $\mathring{a}_{ap}$ and the

refractive index m deduced from the data inversion scheme. As the refractive index is mainly responsible for the variability of $å_{ap}$ of pure dust aerosol, we determined the range of uncertainty of $å_{ap}$ from the variation of the refractive index within one standard deviation of PSAP data averaged over the analysed dust-plume encounter sequence.

Potential error sources of our method are the refractive index value assumption and, to less extent, the measured size distribution. The uncertainties arising from the determination of the refractive index from a set of proxy key components are evaluated in the following. The uncertainties arising from the size distribution are considered as negligible, based on the sensitivity tests reported in the previous section. Additional uncertainty may arise from the fact that the absorption and the scattering coefficients, which are required for the PSAP data inversion according to eq. (2), may differ from the values calculated by Mie theory for spherical particle shape. The latter uncertainty cannot be quantified for non-spherical particles of irregular shape. Recalling that the PSAP instrument measures particles collected on a filter substrate, the assumption that on average randomly oriented irregularly shaped particles can be approximated by a set of spherically shaped particles is justified.

Summarizing, we attribute the uncertainties in the refractive index determination to the appropriate volume mixture of the proxy key compound in the PSAP data inversion schemes. For one exemplary case, Fig. 3 shows the PSAP-signal smoothed by a 10-s moving average (filled symbols, thick solid line), its standard deviation (hatched area), one successful PSAP data inversion (open symbols, thick dashed line) and the scanning of the uncertainty range. Extreme results from the scheme matching the boundaries of the PSAP uncertainty area are considered as the upper and lower limits of possible refractive index values, which still reproduce the observations.

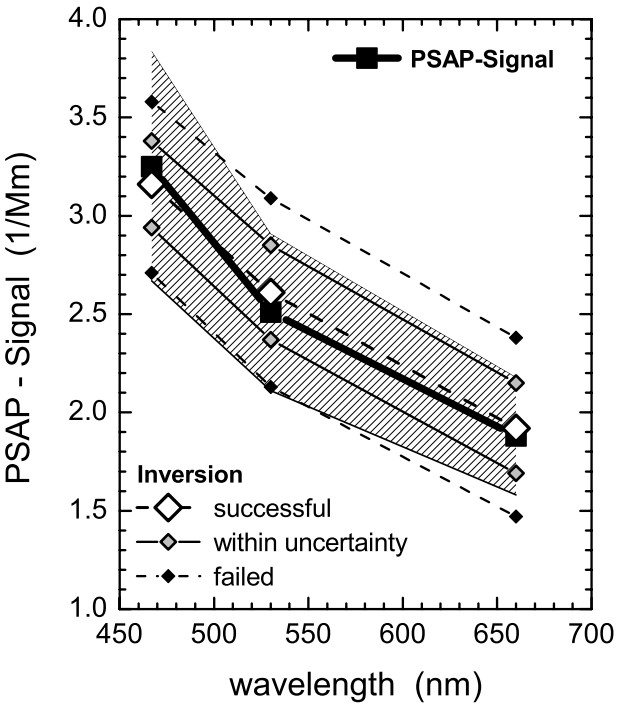

Fig. 3. Uncertainty of the method as determined from the variation of the refractive index within the uncertainty range of the averaged constant-level PSAP data (grey-shaded area).

This approach was applied to selected dust plume encounters that were probed during constant-altitude flight levels. These flight sequences are referred to by the date of the flight and by the running number of the constant-altitude flight sequence. For our tests, we chose levels 060603b/L5 and 060604a/L8 with high $å_{ap}$ values and levels 060520a/L3 and 060603a/L4 with low $å_{ap}$ values. The results are given in Table 1 for the imaginary part of the refractive index. Real parts of the refractive index vary between 1.55 and 1.56. In case of k, relative variations are 10%–16% for values at 450 nm and 25% for values at 700 nm, which, however, are close to the detection limit of the method. Thus, a conservative estimate for the uncertainty of the method is $\pm\Delta å_{ap}/å_{ap} = 20\%$ and $\pm\Delta k/k = 25\%$. Based on a 95% confidence criterion, the PSAP method permits the statistically significant separation of $å_{ap}$ values of 2.0 ± 0.8, 4.0 ± 1.6 and 7.0 ± 2.8. These relative uncertainties of $å_{ap}$ were extrapolated to all other $å_{ap}$ values.

3.2. Stratified dust layer from 3 June 2006

We demonstrate the sensitivity of the PSAP inversion method on the basis of the broad spectrum of absorption Ångström exponents encountered over Ouarzazate and Zagora on the flight 060603b. This flight was conducted in the morning of 3 June between 7:23 and 9:04 UTC, before the onset of convection. Therefore, the stratified structure of the atmosphere was not yet disturbed.

Figure 4a shows the observed two-layer structure with dust from two different source regions deduced from the HSRL backscatter ratio, which is proportional to the concentration of light-scattering particles. Corresponding sequences of flight 060603 are added to Fig. 4a. The elevated dust layer at altitudes >2800 m a.s.l., which can be associated to dust residues from previous days (Knippertz et al., 2008), are labelled Episode 3a over Ouarzazate and Zagora, and Episode 3b north of the Atlas mountains, whereas the dust moved in near ground is labelled Episode 3c. The obtained optical values for $å_{ap}$, as well as the effective diameter $D_{\text{eff,fine mode}}$ of five constant level flight sequences for the flight on 3 June (L3, L4, L5, L6, L8) inside the two dust layers are summarized in Table 2. The absorption Ångström exponent measured in the constant flight levels, performed in the upper dust layer between 2500 and 4000 m, ranges from 3.6 (level L3) to 3.8 (level L6), whereas the absorption Ångström exponents in the dust layer below 2500 m are 6.0 (level L8), 6.5 (level L5) and 6.6 (level L4). The difference in $å_{ap}$ is statistically significant on a 95% confidence level since

Table 1. Absorption Ångström exponent $\mathring{a}_{ap}$, imaginary part of the refractive index k and related uncertainties for selected samples

Level	$\mathring{a}_{ap}$	k ($\lambda = 450$ nm)	k ($\lambda = 700$ nm)	$\pm\Delta\mathring{a}_{ap}/\mathring{a}_{ap}$ (%)	$\pm\Delta k/k$ (%)
060603b/L5	6.5	0.0030	0.0003	<11	<10
	(6.5–8.0)	(0.0027–0.0032)	(0.0001–0.0003)		
060604a/L8	6.1	0.0033	0.0003	4	<10
	(5.7–6.2)	(0.0030–0.0036)	(0.0003–0.0004)		
060520a/L3	3.2	0.0049	0.0017	<19	25
	(2.5–3.7)	(0.0042–0.0067)	(0.0013–0.0025)		
060603a/L4	2.6	0.0038	0.0017	<20	16
	(2.2–3.1)	(0.0032–0.0044)	(0.0013–0.0025)		

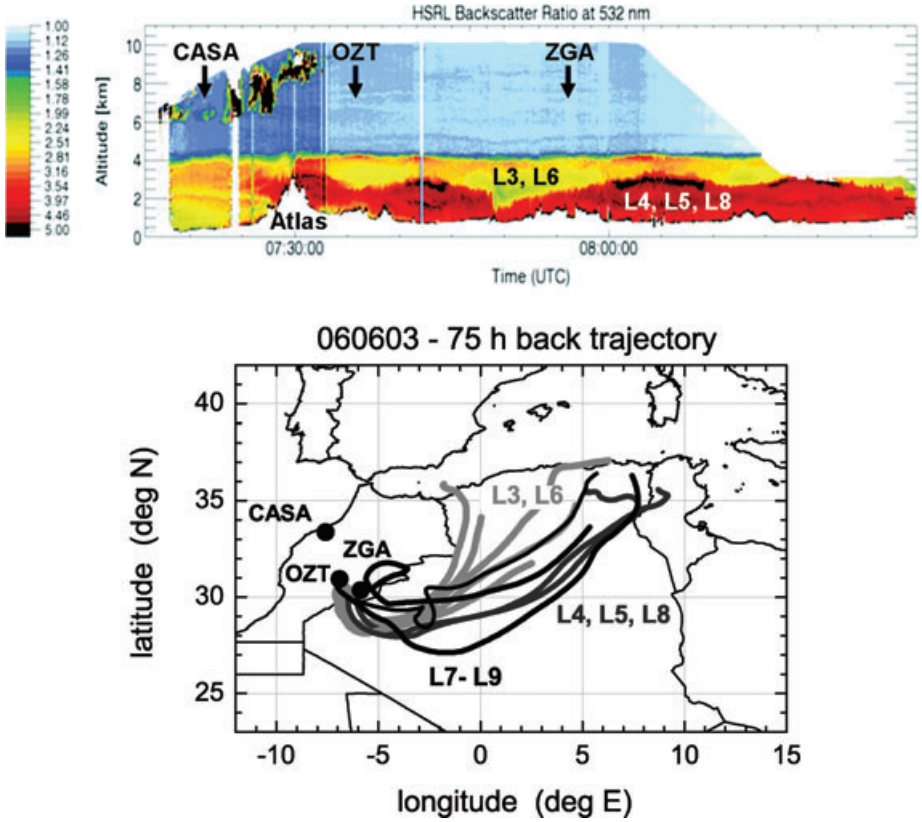

Fig. 4. Episode 3: two-layered dust structure over the ground sites Ouarzazate (OZT) and Zagora (ZGA) with dust from two different source regions and the top layer of dust extending across the Atlas Mountains towards Casablanca (CASA). (A) LIDAR cross-section of the dust layer, including the Labels of the analysed constant levels; (B) 75-h backtrajectories for the respective levels.

their relative deviation is >40%. As is also shown in Table 2, the dust being present in the layer on the following day (4 June) shows no longer a stratified structure but corresponds across the entire layer to the low-layer dust from 3 June with its high $\mathring{a}_{ap}$ value.

Trajectory analyses demonstrate that the dust layers observed on 3 June originate from two different source regions. Figure 4b shows the 75-h backtrajectories, which indicate that the upper dust layer originates from the Atlas forelands between Morocco and Algeria. This dust has been lifted by density currents emanating from thunderstorms over the mountains on 31 May and 2 June (Knippertz et al., 2007). The near-surface air originates from the lowlands and salt lakes in northeastern Algeria and Tunisia, where dust is mobilized in connection with a cold surge from the Mediterranean on 1 June, see Knippertz et al. (2008; Figs. 5 and 6).

3.3. Absorption Ångström exponent and dust refractive index

3.3.1. Absorption Ångström exponent. The full data set of analysed. constant-level sequences consists of 72 samples, of

Table 2. Absorption Ångström exponent ($\mathring{a}_{ap}$) and effective diameter of the fine mode aerosol ($D_{eff,fine\,mode}$) for stratified dust layers on 3 and 4 June 2006, over Ouarzazate and Zagora. Layer numbers refer to the sequences of the flight pattern (see also Fig. 4)

	3 June 2006				4 June 2006			
Layer No.	L3	L4	L5	L6	L8	L7	L8	L9
Layer altitude (m a.s.l.)	3800	2500	1200	3800	2300	3700	1900	1200
$\mathring{a}_{ap}$	3.6	6.6	6.5	3.8	6.0	7.1	6.1	6.5
$D_{eff,fine\,mode}$ (μm)	0.93	1.12	1.13	1.05	1.11	1.06	1.01	1.08

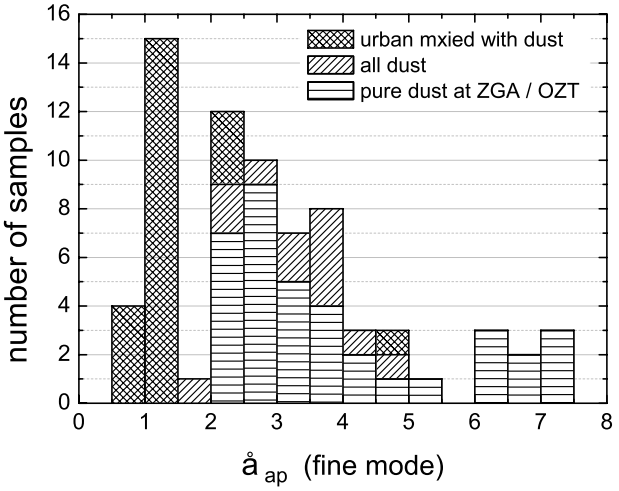

Fig. 5. Number of occurrence for absorption Ångström exponent $\mathring{a}_{ap}$ for all analysed samples, specified according to the samples aerosol type. The 'pure dust' subset samples over Zagora (ZGA) and Ouarzazate (OZT) is restricted to all dust samples taken south of the Atlas Mountains; the 'all dust' subset also includes samples taken north of the Atlas Mountains with potential influence from urban pollution.

which 23 are classified as urban aerosol partially mixed with dust or sea salt, collected at Casablanca airport or in the boundary layer above Casablanca, 37 are classified as pure dust samples taken south of the Atlas Mountains over the ground sites of Ouarzazate and Zagora and 12 are classified as partially polluted dust collected north of the Atlas Mountains, where already some entrainment of anthropogenic pollution might have occurred. The histogram of the full data set is shown in Fig. 5. The anthropogenically polluted layers cluster at $\mathring{a}_{ap} = 1.0$, as is expected from laboratory data for BC dominated aerosol (Schnaiter et al., 2006). The dust samples without anthropogenic pollution show a bi-modal frequency distribution with one group extending from $\mathring{a}_{ap} = 2.0$– to 4.0 and a second group clustering around $\mathring{a}_{ap} = 6.5$. The separation of dust samples from north of the Atlas Mountains does not change this feature significantly.

Separating the dust subset according to dust episodes yields the results displayed in the panels of Fig. 6. Whereas Episodes 1 and 2 are characterized by a small variation of $\mathring{a}_{ap}$, Episode 3 has to be divided into the respective samples taken in the different layers, which were stacked above the ground sites during Episode 3, that is, Levels L3 and L6 are part of Episode 3a, b, whereas Levels L4, L5, and L8 of 3 June and all levels of 4 June are part of Episode 3c.

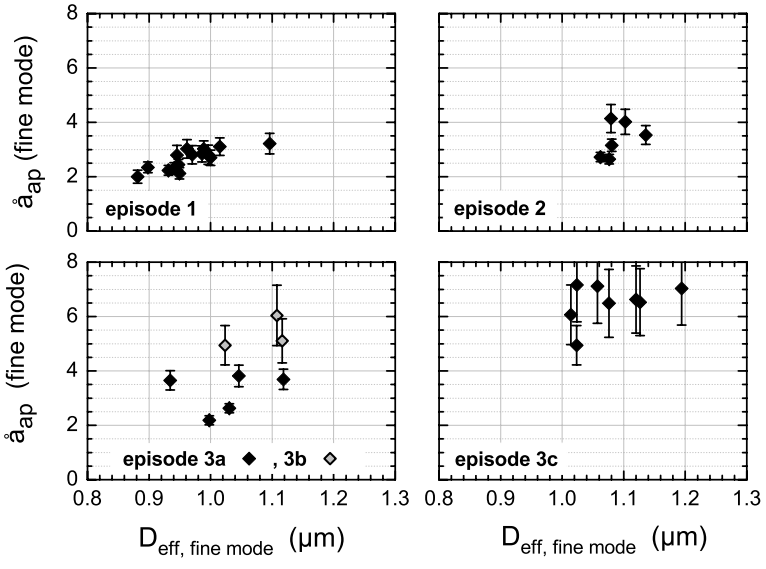

Fig. 6. Absorption Ångström exponent as a function of the effective diameter of the fine mode fraction for the SAMUM data set, plotted separately for the indicated dust episodes; error bars represent the uncertainty in $\mathring{a}_{ap}$, determined by refractive index variations.

Table 3. Average real (n) and imaginary (k) parts of the refractive indices of sampled dust for the individual dust episodes over Morocco; one standard deviation uncertainties are added in parentheses

	Episode 1		Episode 2		Episode 3c	
$\mathring{a}_{ap}$	2.65 (0.38)		3.26 (0.66)		6.72 (0.40)	
λ (nm)	n	k (10^{-3})	n	k (10^{-3})	n	k (10^{-3})
450	1.565	5.2	1.556	3.6	1.550	3.1
	(0.004)	(0.9)	(0.002)	(0.4)	(0.001)	(0.4)
550	1.561	4.2	1.553	2.4	1.549	1.6
	(0.003)	(0.7)	(0.002)	(0.3)	(0.001)	(0.2)
700	1.555	2.5	1.549	1.3	1.546	0.3
	(0.003)	(0.6)	(0.002)	(0.4)	(0.001)	(0.1)

The $D_{\text{eff,fine mode}}$ values, however, are entirely decoupled from the behaviour of I_{ap}, as is already indicated by the values compiled in Table 2. Episode 1 varies over a narrow range of $\mathring{a}_{ap}$ values from 2.0 to 3.25, whereas $D_{\text{eff,fine mode}}$ varies from 0.9 to 1.10 μm. Episodes 2 and 3c are confined with respect to parameters $D_{\text{eff,fine mode}}$ and $\mathring{a}_{ap}$. The variation of ($D_{\text{eff,fine mode}}$, $\mathring{a}_{ap}$) for Episodes 3a and 3b reflects the mixing from dust with properties similar to Episodes 1 and 2 and dust with properties as during Episode 3c.

3.3.2. Complex refractive index and chemical composition. The complex refractive indices associated with the absorption Ångström exponents determined from the PSAP data inversion are summarized in Table 3 for Episodes 1, 2, and 3c. Again, values for Episodes 1 and 2 are indistinguishable in a statistical sense, whereas Episode 3c is characterized by significantly different refractive indices. Table 3 provides that the real part of the refractive index varies neither with wavelength nor with the different dust episodes. Values range from 1.55 to 1.56. The imaginary part, however, differs for Episodes 1 and 2 by an approximate factor of 2.5 from 450 to 700 nm, whereas it differs for Episode 3c by a factor of 10. The dust encountered in Episode 3c is thus very weakly absorbing in the red spectral region, whereas the differences in the blue spectral region compared with the other dust cases are less pronounced and even statistically insignificant for Episodes 2 and 3c.

The average chemical composition for all aerosol samples collected by the Falcon in terms of particle classes (see Kandler et al., 2008) is displayed in Fig. 7, which intends to give an overview of the chemical characteristics of the collected dust particles. Although we used a two-stage impactor for aerosol sampling, dust particles were collected almost exclusively on the second stage of the impactor with a lower cut-off diameter of 1.0 μm. Hence, for the airborne samples, no size-resolved chemical composition is accessible. The silicates class of particles is always dominating, with low variability between the individual samples. Quartz and the calcium-dominated groups show only half of the concentration for airborne samples compared with Tinfou ground station samples (Kandler et al., 2008).

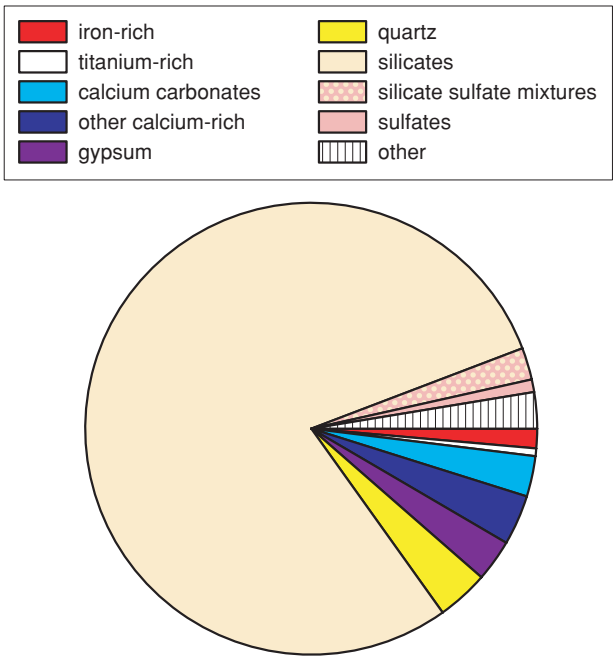

Fig. 7. Average of the chemical composition for all flights derived by single particle analysis, given as total volume fraction of particle classes.

This may result from a well-mixed aerosol, which partly originates from other sources than the dust measured at the ground station. In contrast, the abundances of the iron- and titanium-rich classes are nearly identical to the values found at Tinfou, which may indicate a more homogeneous distribution of the according minerals over the source regions.

Ground based measurements of total dust chemical composition at Tinfou revealed that there are three size regimes in terms of chemical aerosol composition (Kandler et al., 2008). Below 500 nm in particle diameter, the aerosol is composed of mineral dust and sulphate with changing fractions depending on the air mass source. Between 500 nm and 2.5 μm, mineral dust is strongly dominating over the sulphate. Particles larger than 2.5 μm are predominantly mineral dust. The main features of the composition of the mineral dust component as a function of particles size are a mode of calcium-rich particles centred at 3 μm and increasing quartz content for particles larger than 50 μm. Otherwise, the dust volume composition emerged as quite constant over particle size. In particular, the aerosol iron content and the haematite content derived thereof, which determines mineral dust light absorption in the mode used here, are nearly constant for all particle sizes.

The comparison of the imaginary part of the refractive index modelled from the single particle chemical measurements with those calculated from the PSAP inversion algorithm is shown in Fig. 8. For the values derived from the chemical composition, aerosol absorption is attributed exclusively to haematite. For the two shorter wavelengths, a common tendency is present.

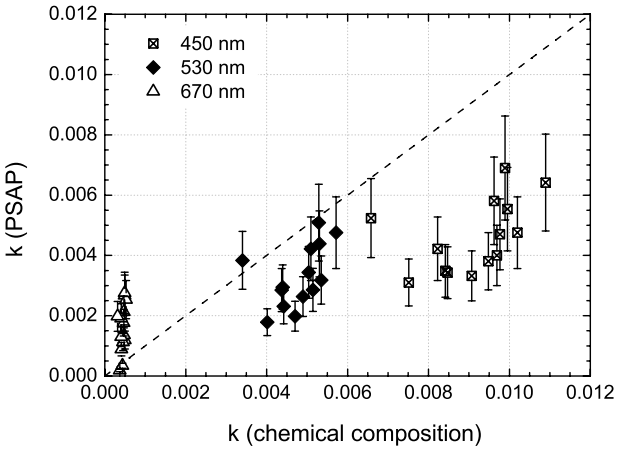

Fig. 8. Comparison of the imaginary part of the refractive indices k, derived from chemical measurements versus those measured by the three wavelengths–PSAP; error bars for k values from the PSAP methods represent the conservative error estimate of 25%.

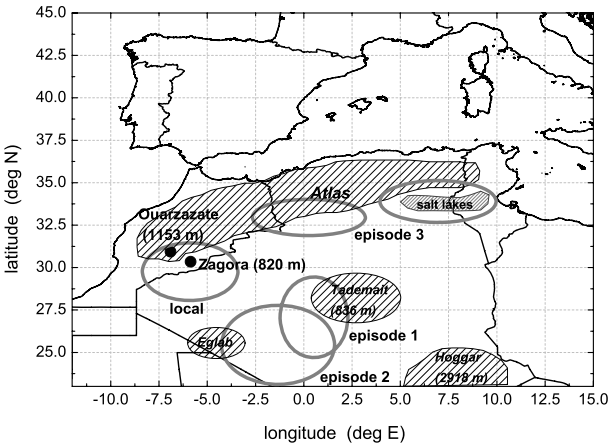

Fig. 9. Source regions of the various dust episodes encountered during the SAMUM research flights.

At wavelengths 450 and 530 nm, linear regression yields a correlation coefficient of greater than 0.7. At 670-nm wavelength, however, nearly no change in the absorption determined by the chemical analysis can be seen, whereas the PSAP measurements clearly exhibit a variation. This is due to the fact, that haematite—the dominating absorbing substance taken into account by the refractive index calculations from the chemical measurements—is only weakly absorbing at this wavelength. Thus, a variation in haematite content does not translate into a strong variation of absorption in the red spectral region.

From these findings, it has to be concluded that another substance with a spectrally flat absorption coefficient is present, which may be minute amounts of BC or kaolinite below the detection limit of the chemical analyses. Assuming an imaginary part of the BC refractive index at 700 nm of 0.63 (Ackerman and Toon, 1981) and attributing aerosol absorption at 700 nm to BC only, BC volume fractions as low as 0.4% (Episode 1) and 0.05% (Episode 3) are calculated from the applied mixing rule (Eq. 1). The general overestimation of absorption at 450-nm wavelength of the chemistry-derived values fits into this scheme, as in this chemistry-based model, all absorption is attributed exclusively to haematite. On the other hand, the optical model based on the PSAP data inversion scheme constructs the refractive index from a linear combination of selected proxies independent of their abundances. The combination of both complementary methods supports the conclusion that in the SAMUM cases, dust absorption is not only caused by haematite but also by another compound with a less pronounced spectral dependence of the complex refractive index.

3.4. Source regions

The dust source region may influence $\mathring{a}_{ap}$ and $k(\lambda)$ via the chemical composition and the microphysical properties of the mobilized dust. Assuming that the mineralogical composition of the airborne dust particles does not change significantly during the atmospheric transport, the refractive index depends mainly on the soil chemical composition of the source region. A potential effect of the observed coating of the particles on dust properties can be excluded in our cases, since the coating was observed only on the smaller accumulation mode particles, which had only a minor influence on the overall optical properties of the sampled dust. We identified the source regions shown in Fig. 9 by exploiting LAGRANTO backward trajectories, ECMWF wind field analyses, MSG satellite scenes and WMO dust storm reports.

During Episode 1, the dust originated from various nearby sources south of the measurement area. The synoptic analysis (Knippertz et al., 2008) characterizes the episode as dominated by a persistent surface high and locally generated dry-convective dust plumes. During Episode 2, characterized by low absorption Ångström exponents, we identify a dust source region almost identical to Episode 1, that is, sources were situated south and east of the field sites. Two regionally different dust sources existed in Episode 3. On one hand, dust aerosol with low absorption Ångström exponents (Episode 3a) originated from the Atlas forelands between Algeria and Morocco. On the other hand, dust aerosol with high absorption Ångström exponents (Episode 3c) originated from the lowlands and lakes in northeastern Algeria and Tunisia. In all episodes dust may also come from regional sources. These regions have been identified as dust sources by Caquineau et al. (2002).

4. Comparison of results to data from SAMUM and from literature

The results obtained from the analysis of the SAMUM field data provide an extensive set of optical data of desert dust aerosol, which have to be compared with data reported from other measurements during SAMUM and with data in the literature.

Referring to the complex refractive index results from SAMUM partners first, the values deduced from the PSAP data inversion scheme are supported by results from the chemical analysis of simultaneously collected airborne dust samples. The deviations between the complementary methods of chemical analyses and optical analyses indicate the presence of a particulate absorber, which is below the detection limit of the analysis methods. The complex refractive index determined from the chemical composition for ground-based samples at Tinfou (Kandler et al., 2008) is characterized by a real part varying from 1.55 to 1.56 at 530 nm, which is in close agreement with our observations of 1.55–1.56. The imaginary part of the refractive index for the samples collected near ground over Zagora/Tinfou is $k = 1.8 \times 10^{-3}$–3.1×10^{-3}, which again is close to the results from our method scattering around 3×10^{-3}–4×10^{-3} for airborne samples collected above Zagora/Tinfou.

The imaginary part of refractive indices derived from ground-based simultaneous measurements of optical properties σ_{sp} and i_{ap} and of particle size distributions at the Tinfou site ranges for a wavelength of 530 nm from 4.2×10^{-3} on 22 May to 5.9×10^{-3} on 28 May and to 3.3×10^{-3} on 4 June (Schladitz et al., 2008). Another optical method, based on spectral aerosol absorption measurements (Müller et al., 2008) from samples taken at the same sampling site yields a value of 4.0×10^{-3} for 22 May. The respective values at 530 nm from the Falcon airborne samples at 500 m above ground for the same time periods are 3.4×10^{-3} (22 May), 2.3×10^{-3} (28 May) and 2.3×10^{-3} (4 June). The values from the ground-based data are systematically higher than the values from the airborne samples. One potential reason might be that the ground-based samples are influenced by low levels of anthropogenic pollution from nearby sources, which can be excluded for the airborne samples.

Sun photometer and lidar data from the ground site Ouarzazate were used as well for calculating dust refractive indices (D. Müller, private communication). For the Falcon overflight on 19 May, they found a real part of the refractive index of 1.45, independent of the wavelength, which is significantly lower than the value of 1.55 from the airborne samples. The imaginary component of the refractive index at 530 nm is 4×10^{-3}–5×10^{-3}, which is similar to the value of the airborne sample of 4.2×10^{-3}–4.4×10^{-3}. The reason behind the significant difference in the real part of the refractive index is currently under investigation.

The entire set of k values deduced from PSAP data compared with literature data is shown in Fig. 10. Our refractive index data fall in between sun photometry data and data used in databases. The values taken from Shettle and Fenn (1979) and from d'Almeida et al. (1991) tend to overestimate the light absorption by dust significantly, whereas the sun photometry values (Dubovik et al., 2002; Todd et al., 2007) coincide with the lower bound of our observations.

5. Summary and conclusions

As part of the SAMUM, the complex refractive index of desert dust was determined from airborne in situ measurements of particle size distributions in the diameter size range $4 \leq D_p \leq 100\,\mu$m and of aerosol absorption coefficients at three different wavelengths in the blue (467 nm), green (530 nm) and red (660 nm) spectral regions. A new data analysis scheme was developed, which combines aerosol absorption data measured by means of a PSAP and size distribution data measured by CPC and optical particle counters. The vertical structure of the investigated dust layers was analysed by an airborne HSRL, which measures aerosol extinction directly. The origin of the

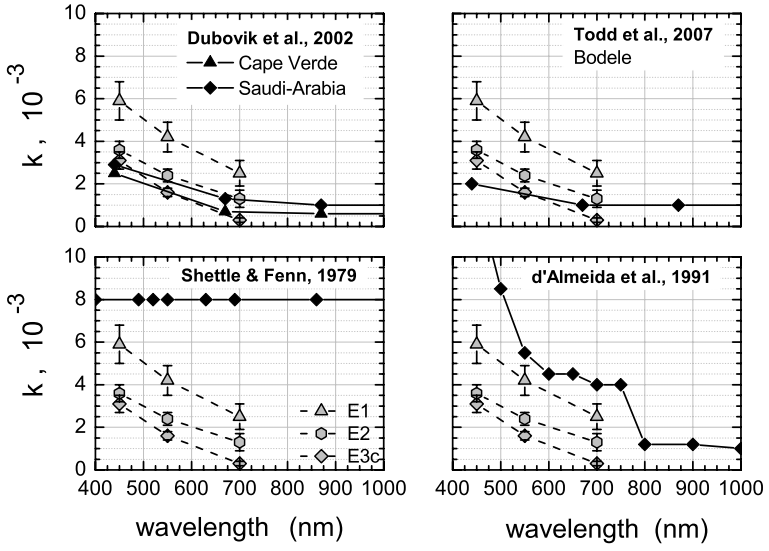

Fig. 10. Imaginary part of the refractive index k from SAMUM as a function of wavelength; reference data from literature refer to AERONET (Dubovik et al., 2002), sun photometry (Todd et al., 2007), a review of laboratory studies (Shettle and Fenn, 1979) and the OPAC data set (d'Almeida et al., 1991).

investigated dust layers was estimated from trajectory analyses combined with MSG scenes and wind field data analyses.

The real part n of the dust refractive index is found almost constant with values between 1.55 and 1.56, independent of the wavelength. In contrast, the imaginary part k of the refractive index shows strong variations between different dust episodes and also across the investigated spectral region. Our analyses yield a significant variability of dust optical properties for different dust source regions. The refractive index data, however, are confirmed by data calculated from the chemical analysis of simultaneously collected dust samples. A comparison with refractive index data reported in the literature demonstrates that values derived from sun photometry tend to underestimate the imaginary part of the refractive index, whereas values from laboratory studies tend to overestimate the value. For future measurements of the chemical composition and of related optical properties, particular attention has to be paid to other light-absorbing aerosol components besides haematite, for example, the presence of soot or other iron-containing compounds.

Because of the influence of dust origin on the refractive index, we hesitate to state an average dust refractive index for dust from the northwestern Sahara. Moreover, the presented data analysis demonstrates the necessity for considering dust sources carefully, if dust radiative properties are used in radiative transfer calculations. Radiative transfer issues, however, are beyond the scope of this study. They are treated in detail in separate SAMUM publications (Bierwirth et al., 2008; Otto et al., 2008).

6. Acknowledgments

The SAMUM research group is funded by the German Science Foundation (DFG) under Grant FOR 539. We also received support from the European Space Agency under ESA Contract No. 19429/06/NL/AR. Furthermore, we are grateful to the DLR flight operations crew (Stefan Grillenbeck, Steffen Gemsa, Christian Hinz, Heinz Finkenzeller) for their perfect collaboration during the experiment and to Hermann Mannstein and Waldemar Krebs (both DLR) for providing the MSG data. The operation of the Falcon would also not have been possible without the full support from Royal Air Maroc, who hosted us in their facilities in Casablanca during the experiments, and from the DLR Space Programme, which contributed a significant amount to the Falcon operation budget. Finally, we thank Hans Rüba, Andreas Fix, Christoph Kiemle and Martin Wirth (all from DLR) for their assistance during the field experiment phase and the data analysis of SAMUM. The detailed comments of two anonymous reviewers are gratefully acknowledged as well.

References

Ackerman, T. P. and Toon, O. B. 1981. Absorption of visible radiation in atmosphere containing mixtures of absorbing and nonabsorbing particles. *Appl. Opt.* **20**, 3661–3668.

Alfaro, S. C., Lafon, S., Rajot, J. L., Formenti, P., Gaudichet, A. and co-authors. 2004. Iron oxides and light absorption by pure desert dust: an experimental study. *J. Geophys. Res.* **109**, 1–9.

Angström, A. 1964. The parameters of atmospheric turbidity. *Tellus* **16**, 64–75.

Arakawa, E. T., Tuminello, P. S., Khare, B. N., Millham, M. E., Authier, S. and co-authors. 1997. Measurement of optical properties of small particles, ORNL/CP–95872, Oak Ridge National Lab, United States.

Balkanski, Y., Schulz, M., Claquin, T. and Guibert, S. 2007. Reevaluation of Mineral aerosol radiative forcings suggests a better agreement with satellite and AERONET data. *Atmos. Chem. Phys.* **7**, 81–95.

Bergstrom, R. W., Pilewskie, P., Pommier, J., Rabbette, M., Russell, P. B. and co-authors. 2004. Spectral absorption of solar radiation by aerosols during ACE-Asia. *J. Geophys. Res.* **109**, 1–13.

Bierwirth, E., Wendisch, M., Ehrlich, A., Heese, B., Otto, S. and co-authors. 2008. Spectral surface albedo over Morocco and its impact on the radiative forcing of saharan dust. *Tellus* **61B**, doi: 10.1111/j.1600-0889.2008.00395.x.

Bohren, C. F. and Huffman, D. R. 1983. *Absorption and Scattering of Light by Small Particles.* John Wiley & Sons, Inc., New York.

Bond, T. C., Anderson, T. L. and Campbell, D. 1999. Calibration and intercomparison of filter-based measurements of visible light absorption by aerosols. *Aerosol Sci. Technol.* **30**, 582–600.

Caquineau, S., Gaudichet, A., Gomes, L. and Legrand, M. 2002. Mineralogy of Saharan dust transported over northwestern tropical Atlantic Ocean in relation to source regions. *J. Geophys. Res.* **107**, 4251, doi: 10.1029/2000JD000247.

Cattrall, C., Carder, K. L. and Gordon, H. R. 2003. Columnar aerosol single-scattering albedo and phase function retrieved from sky radiance over the ocean: measurements of Saharan dust. *J. Geophys. Res.* **108**, 4287, doi: 10.1029/2002JD002497.

d'Almeida, G. A., Koepke, P. and Shettle, E. P. 1991. *Atmospheric Aerosols: Global Climatology and Radiative Characteristics*. A. Deepak Publishing, Hampton, VA.

Dubovik, O., Holben, B., Eck, T. F., Smirnov, A., Kaufman, Y. J. and co-authors. 2002. Variability of Absorption and Optical Properties of Key Aerosol Types Observed in Worldwide Locations. *J. Atmos. Sci.* **59**, 590–608.

Esselborn, M., Wirth, M., Fix, A., Tesche, M. and Ehret, G. 2007. Airborne high spectral resolution lidar for measuring aerosol extinction and backscatter coefficients. *Appl. Opt.* **47**, 346–358.

Feldpausch, P., Fiebig, M., Fritzsche, L. and Petzold, A. 2006. Measurement of ultrafine aerosol size distributions by a combination of diffusion screen separators and condensation particle counters. *J. Aerosol Sci.* **37**, 577–597.

Fiebig, M., Stein, C., Schröder, F., Feldpausch, P. and Petzold, A. 2005. Inversion of data containing information on the aerosol particle size distribution using multiple instruments. *J. Aerosol Sci.* **36**, 1353–1372.

Haywood, J. M., Francis, P. N., Glew, M. D. and Taylor, J. P. 2001. Optical properties and direct radiative effect of Saharan dust: a case study of two Saharan dust outbreaks using aircraft data. *J. Geophys. Res.* **106**, 18 417–18 430.

Haywood, J., Francis, P., Osborne, S., Glew, M., Loeb, N. and co-authors. 2003. Radiative properties and direct radiative effect of Saharan dust measured by the C-130 aircraft during SHADE, 1: solar spectrum. *J. Geophys. Res.* **108**, 8577, doi: 10.1029/2002JD002687.

Heintzenberg, J. 2008. The SAMUM-1 experiment over Southern Morocco: Overview and introduction. *Tellus* **61B**, doi: 10.1111/j.1600-0889.2008.00403.x.

Kaaden, N., Massling, A., Schladitz, A., Müller, T., Kandler, K. and co-authors. 2008. State of Mixing, Shape Factor, Number Size Distribution, and Hygroscopic Growth of the Saharan Anthropogenic and Mineral Dust Aerosol at Tinfou, Morocco. *Tellus* **61B**, doi: 10.1111/j.1600-0889.2008.00388.x.

Kandler, K., Benker, N., Bundke, U., Cuevas, E., Ebert, M. and co-authors. 2007. Chemical composition and complex refractive index of Saharan Mineral Dust at Izaña, Tenerife (Spain) derived by electron microscopy. *Atmos. Environ.* **41**, 8056–8074.

Kandler, K., Schütz, L., Deutscher, C., Hofmann, H., Jäckel, S. and co-authors. 2008. Size distributions, mass concentrations, chemical and mineral composition and optical parameters of the boundary layer aerosol at Tinfou, Morocco, during SAMUM 2006. *Tellus* **61B**, doi: 10.1111/j.1600-0889.2008.00385.x.

Knippertz, P., Deutscher, D., Kandler, K., Müller, T., Schulz, O. and co-authors. 2007. Dust mobilization due to density currents in the Atlas region: observations from the SAMUM 2006 field campaign. *J. Geophys. Res.* **112**, D21109.

Knippertz, P., Ansmann, A., Althausen, D., Müller, D., Tesche, M. and co-authors. 2008. Dust Mobilization and Transport in the Northern Sahara during SAMUM 2006 - A Meteorological Overview. *Tellus* **61B**, doi: 10.1111/j.1600-0889.2008.00380.x.

Lafon, S., Sokolik, I. N., Rajot, J. L., Caquineau, S. and Gaudichet, A. 2006. Characterization of iron oxides in mineral dust aerosols: implications for light absorption. *J. Geophys. Res.* **111**, 1–19.

Liao, H. and Seinfeld, J. H. 1998. Radiative forcing by mineral dust aerosols: sensitivity to key variables. *J. Geophys. Res.* **103**, 31 637–31 646.

Linke, C., Möhler, O., Veres, A., Mohácsi, Á., Bozóki, Z. and co-authors. 2006. Optical properties and mineralogical composition of different Saharan mineral dust samples: a laboratory study. *Atmos. Chem. Phys.* **6**, 3315–3323.

McFarquhar, G. M. and Heymsfield, A. J. 1998. The Definition and Significance of an Effective Radius for Ice Clouds. *J. Atmos. Sci.* **55**, 2039–2052.

Müller, T., Schladitz, A., Kaaden, N. and Wiedensohler, A. 2008. Spectral absorption coefficients and imaginary parts of refractive indices of Saharan dust during SAMUM-1. *Tellus* **61B**, doi: 10.1111/j.1600-0889.2008.00399.x.

Myhre, G. and Stordal, F. 2001. Global sensitivity experiments of the radiative forcing due to mineral aerosols. *J. Geophys. Res.* **106**, 18 193–18 204.

Otto, S., Bierwirth, E., Weinzierl, B., Kandler, K., Esselborn, M. and co-authors. 2008. Solar radiative effects of a Saharan dust plume observed during SAMUM assuming non-spherical dust particle. *Tellus* **61B**, doi: 10.1111/j.1600-0889.2008.00389.x.

Ouimette, J. R. and Flagan, R. C. 1982. The extinction coefficient of multicomponent aerosols. *Atmos. Environ.* **16**, 2405–2419.

Patterson, E. M., Gillette, D. A. and Stockton, B. H. 1977. Complex index of refraction between 300 and 700 nm for Saharan aerosols. *J. Aerosol Sci.* **82**, 3153–3160.

Petzold, A., Fiebig, M., Flentje, H., Keil, A., Leiterer, U. and co-authors. 2002. Vertical variability of aerosol properties observed at a continental site during the Lindenberg Aerosol Characterization Experiment (LACE 98). *J. Geophys. Res.* **107**, LAC10-11–LAC10-18.

Schladitz, A., Müller, T., Massling, A., Kaaden, N., Kandler, K. and co-authors. 2008. In situ measurements of Optical Properties at Tinfou (Morocco) during the Saharan Mineral Dust Experiment SAMUM 2006. *Tellus* **61B**, doi: 10.1111/j.1600-0889.2008.00397.x.

Schnaiter, M., Gimmler, M., Llamas, I., Linke, C., JÃ¤ger, C. and co-authors. 2006. Strong spectral dependence of light absorption by organic carbon particles formed by propane combustion. *Atmos. Chem. Phys.* **6**, 2981–2990.

Shettle, E. P. and Fenn, R. W. 1979. Models for the aerosols of the lower atmosphere and the effects of humidity variations on their optical properties, *AFGL-TR-79-0214*, Air Force Cambridge Research Laboratory.

Sokolik, I. N. and Toon, O. B. 1996. Direct radiative forcing by anthropogenic airborne mineral aerosols. *Nature* **381**, 681–683.

Sokolik, I. N. and Toon, O. B. 1999. Incorporation of mineralogical composition into models of the radiative properties of mineral aerosol from UV to IR wavelengths. *J. Geophys. Res.* **104**, 9423–9444.

Sokolik, I. N., Toon, O. B. and Bergstrom, R. W. 1998. Modeling the rediative characteristics of airborne mineral aerosols at infrared wavelengths. *J. Geophys. Res.* **103**, 8813–8826.

Tanré, D., Haywood, J., Pelon, J., Léon, J. F., Chatenet, B. and co-authors. 2003. Measurement and modeling of the Saharan dust radiative impact: overview of the Saharan dust experiment (SHADE). *J. Geophys. Res.* **108**, 8574, doi: 10.1029/2002JD003273.

Tegen, I. and Lacis, A. A. 1996. Modeling of particle size distribution and its influence on the radiative properties of mineral dust aerosol. *J. Geophys. Res.* **101**, 19 237–19 244.

Tegen, I., Lacis, A. A. and Fung, I. 1996. The influence on climate forcing of mineral aerosols from disturbed soils. *Nature* **380**, 419–422.

Tesche, M., Ansmann, A., Müller, D., Althausen, D., Heese, B. and co-authors. 2008. Vertical profiling of Saharan dust with Raman lidars and airborne high-spectral-resolution lidar during SAMUM. *Tellus* **61B**, doi: 10.1111/j.1600-0889.2008.00390.x.

Todd, M. C., Washington, R., Martins, J. V., Dubovik, O., Lizcano, G. and co-authors. 2007. Mineral dust emission from the Bodélé Depression, northern Chad, during BoDEx 2005. *J. Geophys. Res.* **112**, 1–12.

Toon, O. B. and Ackerman, T. P. 1981. Algorithms for the calculation of scattering by stratified spheres. *Appl. Opt.* **20**, 3657–3660.

Virkkula, A., Ahlquist, N. C., Covert, D. S., Arnott, W. P., Sheridan, P. J. and co-authors. 2005. Modification, calibration and a field test of an instrument for measuring light absorption by particles. *Aerosol Sci. Technol.* **39**, 68–83.

Virkkula, A., Koponen, I. K., Teinilä, K., Hillamo, R., Kerminen, V. M. and co-authors. 2006. Effective real refractive index of dry aerosols in the Antarctic boundary layer. *Geophys. Res. Lett.* **33**, 1–4.

Weinzierl, B., Petzold, A., Esselborn, M., Wirth, M., Rasp, K. and co-authors. 2008. Airborne measurements of dust layer properties, particle size distribution and mixing state of Saharan dust during SAMUM 2006. *Tellus* **61B**, doi: 10.1111/j.1600-0889.2008.00392.x.

Wernli, H. and Davies, H. C. 1997. A lagrangian-based analysis of extratropical cyclones, I: the method and some applications. *Q. J. R. Meteorol. Soc.* **123**, 467–489.